

Article

Inhibited Surface Diffusion in Nanoporous Multi-Principal Element Alloy Thin Films Prepared by Vacuum Thermal Dealloying

Tibra Das Gupta  and Thomas John Balk * 

Department of Chemical and Materials Engineering, University of Kentucky, Lexington, KY 40506, USA; tibradasgupta@uky.edu

* Correspondence: john.balk@uky.edu; Tel.: +1-859-257-4582

Abstract: Nanoporous structures with 3D interconnected networks are traditionally made by dealloying a binary precursor. Certain approaches for fabricating these materials have been applied to refractory multi-principal element alloys (RMPEAs), which can be suitable candidates for high-temperature applications. In this study, nanoporous refractory multi-principal element alloys (np-RMPEAs) were fabricated from magnesium-based thin films (VMoNbTaMg) that had been prepared by magnetron sputtering. Vacuum thermal dealloying (VTD), which involves sublimation of a higher vapor pressure element, is a novel technique for synthesizing nanoporous refractory elements that are prone to oxidation. When VMoNbTaMg was heated under vacuum, a nanoporous structure was created by the sublimation of the highest vapor pressure element (Mg). X-ray photoelectron spectroscopy depth profiling indicated significantly less ligament oxidation during VTD as compared to traditional dealloying methods. Furthermore, np-RMPEAs exhibited outstanding stability against coarsening, retaining smaller ligaments (~25 nm) at elevated temperature (700 °C) for a prolonged period (48 h).

Keywords: vacuum thermal dealloying; multi-principal element alloy; nanoporous; surface diffusion



Citation: Das Gupta, T.; Balk, T.J. Inhibited Surface Diffusion in Nanoporous Multi-Principal Element Alloy Thin Films Prepared by Vacuum Thermal Dealloying. *Metals* **2024**, *14*, 289. <https://doi.org/10.3390/met14030289>

Academic Editors: Zhifeng Wang and Qibo Deng

Received: 19 January 2024

Revised: 22 February 2024

Accepted: 26 February 2024

Published: 29 February 2024



Copyright: © 2024 by the authors. Licensee MDPI, Basel, Switzerland. This article is an open access article distributed under the terms and conditions of the Creative Commons Attribution (CC BY) license (<https://creativecommons.org/licenses/by/4.0/>).

1. Introduction

Porous materials with nanoscale features exhibit distinct characteristics as compared to their bulk counterparts, e.g., a high surface-area-to-volume ratio. This makes nanoporous (np) materials promising for a wide range of applications, including catalysis, gas sensing and separation, biosensors, medical applications, energy storage, fuel cell technology, radiation tolerance, etc. [1–7]. These diverse applications offer ample opportunities for scientists to explore novel strategies and techniques for synthesizing such materials.

Typically, np-materials are fabricated by a dealloying process that involves selectively removing an element from a precursor alloy. According to Rugolo et al. [8], dealloying is particularly effective in achieving a uniform nanoporous structure when the precursor alloy system exhibits minimal phase separation, or even better, if it is a homogenous solid solution. Consequently, many np-structures reported previously have been fabricated from single-phase solid solution precursor alloys [9–11]. While it is relatively easy to identify homogenous solid solutions for certain binary alloy systems, the suitable precursor possibilities are limited. Moreover, the complexity of traditional chemical or electrochemical dealloying increases significantly for precursor alloys with three or more elements. Recently, an emerging class of alloys has become increasingly popular: multi-principal element alloys (MPEAs). Unlike typical alloys with one or two major components, MPEAs have four or more major components, with the concentration of each element varying between 5 and 35 at.% [12,13]. MPEAs increase the configurational entropy [12], leading to enhanced thermodynamic stability with minimal phase separation, at least in theory [12]. There are several MPEA systems in which the elements form a single-phase solid solution. Importantly, certain MPEAs exhibit excellent mechanical properties such as high strength and

fracture toughness [14–17], fatigue and creep resistance [18–20], extraordinary corrosion resistance in harsh environments [21–24], and irradiation resistance [25–28].

Np-materials composed of MPEAs are attractive candidates for these applications due to their enhanced surface area [29,30]. Moreover, MPEAs offer an extensive range of unexplored compositions and phase spaces, providing virtually limitless opportunities for suitable precursors. Very recently, there have been several attempts to fabricate nanoporous high entropy alloy (np-HEA) materials that showed improved performance in catalysis [31–34], oxygen evolution and reduction reaction [35–39], and hydrogen evolution reaction [40–42].

Conventional np-materials experience significant ligament coarsening at elevated temperatures due to increased diffusion, leading to the decreased stability of the pore-ligament structure and degraded physical properties [43–46]. Refractory MPEAs potentially offer an effective solution to resist this tendency to coarsen. Combining different elements in a solid solution may lead to decreased diffusion due to atomic size mismatch and high activation energy resulting from fluctuations in lattice potential energy [47–49]. It was reported by Joo et al. [49] that nanoporous Ti-V-Nb-Mo-Ta, synthesized via liquid metal dealloying, retains smaller ligament sizes at high temperatures compared to other, more conventional, np-systems. Another investigation by Okulov et al. [50] with a slightly different nanoporous Ta-Mo-Nb-V-Ni alloy also supports the notion of stability against thermal coarsening. These studies indicate that refractory np-MPEAs have a potential for application in high-temperature and radiation environments [51,52] without the significant degradation of physical properties [53–55].

Common dealloying methods, such as electrochemical dealloying (ECD) and liquid metal dealloying (LMD), face inherent challenges in the processing of certain materials. ECD requires a significant difference in reduction potential between sacrificial and retained elements, and chemical waste (acid containing the sacrificial metal) is generated as a byproduct [56,57]. LMD requires very high temperature(s) for removing sacrificial elements and often requires the use of an etchant to remove the dealloying medium (metal bath material) after it has solidified. Furthermore, certain metallic baths used in LMD pose safety risks, e.g., molten Mg. Finally, np metals and alloys prepared by ECD and LMD are susceptible to oxidation due to the reactivity of the metal ligaments (V, Ti, Mo, Ta, W, etc.).

In this study, we propose the utilization of a novel dealloying technique, vacuum thermal dealloying (VTD), which proceeds at lower temperatures than those used for LMD and also avoids the generation of hazardous waste (used acid) that is inherent to ECD. Because the VTD process is performed in vacuum, oxidation is significantly minimized compared to conventional dealloying methods. Our objective was to synthesize refractory np-MPEA from VMoNbTa-Mg precursor thin film samples using vacuum thermal dealloying with Mg as a sacrificial element. As shown in Figure 1, Mg has a significantly higher vapor pressure compared to the other elements in the MPEA, and this holds over a large temperature range. Therefore, by heating precursor samples in vacuum, Mg should sublime and facilitate the formation of a nanoporous structure via local surface diffusion. Precursor thin films were deposited on Si substrates by magnetron sputtering. The resulting nanoporous structure of refractory alloys fabricated by vacuum thermal dealloying offers potential improvements with respect to improved thermal stability and corrosion resistance. After dealloying, the np-MPEA samples were characterized using electron microscopy, X-ray diffraction, and X-ray photoelectron spectroscopy. The thermal stability of ligaments was investigated by heating the porous alloys at 700 °C for a prolonged period (48 h).

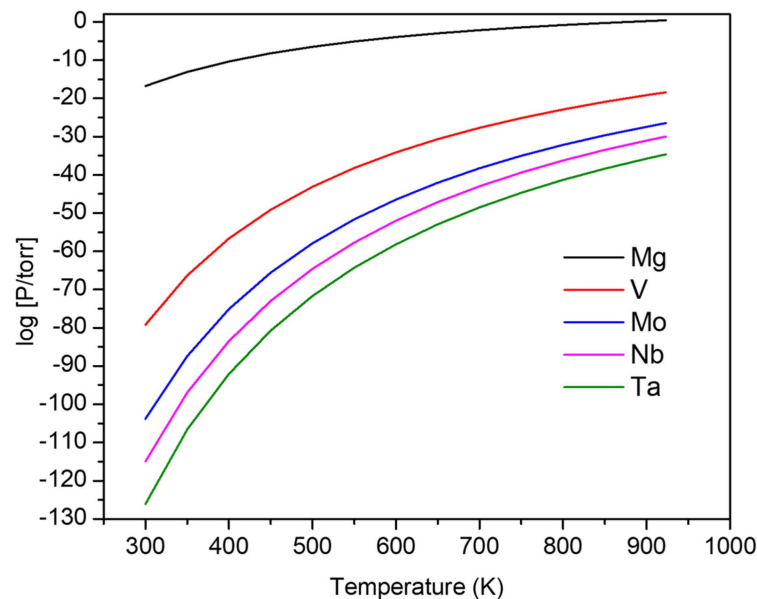


Figure 1. Comparison of vapor pressures for the constituent elements in precursor alloys, with Mg having the highest vapor pressure across a broad temperature range. This graph was generated using equations found in reference [58].

2. Materials and Methods

The deposition of precursor thin films was performed in an ORION magnetron sputtering system (AJA International, Inc.; Hingham, MA, USA) with a main chamber base pressure of 10^{-8} torr. Small pieces of 100-oriented Si wafer were used as substrate and were cleaned by RF biasing for 90 s at 2.5×10^{-2} torr prior to deposition. Argon was used as the process gas at a pressure of 2.7×10^{-3} torr. This pressure was selected to minimize stress in the as-deposited thin films on Si and was determined by depositing individual films onto thin Kapton substrates at pressures ranging from 2.4×10^{-3} to 2.9×10^{-3} torr, followed by visual inspection of induced curvature after release from the specimen carrier plate. High-purity metal targets were used for the deposition of the films: V (99.8%), Mo (99.97%), Nb (99.98%), Ta (99.99%), and Mg (99.95%). Prior to each alloy film deposition, a 10 nm Ta interlayer was deposited for promotion of adhesion between the substrate and alloy film. Precursor alloy composition was optimized by combinatorial screening of a composition gradient film that was deposited onto a stationary substrate. This gradient sample was thermally dealloyed, as described below, to identify regions with the desired nanoporous structure and correlate these with the precursor composition(s) that lead to the preferred structure. Subsequent films with a targeted single composition were achieved by depositing for 20 min onto a rotating substrate.

The thermal dealloying process was performed in the main chamber of the high vacuum sputter deposition system (10^{-7} torr), using a quartz heater (AJA model SHQ-X) attached to the system. Precursor alloy film samples were heated at 10 °C/min ramp rate to 600 °C and were held there for 2 h. At this temperature, the vapor pressure of Mg is significantly higher than that of the other (refractory) metals in the precursor, facilitating sublimation of the sacrificial element Mg from the precursor thin film. It should be noted that the sample temperature may be ~ 50 °C lower than the quartz lamp temperature setpoint. Considering the large size of the main chamber compared to the sample dimensions, saturation of Mg in a vapor above the film is expected to be negligible, and the partial pressure of gaseous Mg was not expected to approach the vapor pressure where simultaneous sublimation and deposition (de-sublimation) might occur. After thermal dealloying, film samples were allowed to cool naturally to room temperature.

Following dealloying, samples were characterized in a focused ion beam and scanning electron microscope (FIB-SEM; FEI Helios 660 dual-beam system; Hillsboro, OR, USA),

including composition analysis by X-ray energy dispersive spectroscopy (EDS; Oxford Instruments X-Max 80 mm² detector; Concord, MA, USA). The composition of certain samples was corroborated by separate EDS measurements (FEI Quanta SEM equipped with Oxford Instruments X-Max 50 mm² detector). Depth profiling of dealloyed film composition was performed using X-ray photoelectron spectroscopy (XPS; Thermo Scientific K-Alpha™; Madison, WI, USA) with a micro-focused monochromatic Al K α ($h\nu = 1486.6$ eV) X-ray source and an EX06 ion source (applied spot size: 200 μm). The peak fitting analysis for XPS spectra was completed using Avantage Data System software. The distribution of ligament widths in dealloyed np samples was measured from plan-view and cross-section images that were analyzed with ImageJ software (version 1.54f). Calibration of the measurement scale was performed in ImageJ using the scale bar from SEM images. Subsequently, a straight line was drawn along the narrowest region in the middle of each ligament in an image, and the measurement function was applied to determine ligament width. Redundant measurements were avoided by annotating ligaments that had already been measured. For each unique annealed sample condition, the average and standard deviation were calculated from the histogram of ligament width measurements. In each case, at least 400 ligaments were measured to minimize error due to data scatter. Crystal structure in precursor and dealloyed samples was investigated by X-ray diffraction (XRD) using a Siemens D500 diffractometer (Cu K α radiation, $\lambda = 1.5406$ Å).

High-temperature heating for long duration was performed on a heating stage inside a custom-built high-vacuum chamber (10^{-6} torr base pressure, with pressure remaining below 10^{-5} torr during dealloying experiments). The temperature of heated samples was measured using an infrared camera (Optris Xi400; Portsmouth, NH, USA).

3. Results and Discussion

3.1. Parting Limit for Successful Dealloying and Formation of Nanoporous Structure

To obtain the desired nanoporous structure, it is crucial to maintain the concentration of the sacrificial element Mg in the precursor alloy at an optimum level [59,60], which is typically near the parting limit, X_p [61,62]. Below this threshold, X_p , the less noble element(s) will not be sufficiently interconnected for effective dealloying and the creation of a bicontinuous nanoporous structure. Conversely, if the concentration of sacrificial element(s) significantly exceeds the parting limit X_p , film cracking will occur. The (VMoNbTa)-Mg precursor alloy system was investigated via combinatorial screening of a composition gradient film, as described above. Based on a comparison of thermally dealloyed film regions and the precursor alloy composition in those regions, it was determined that the parting limit X_p for Mg lies in the range of 75–80 at.%. The plan-view and cross-section images of nanoporous structure from a precursor sample with optimized composition (VMoNbTa)₂₄Mg₇₆ are shown in Figure 2.

Excessive Mg content in the precursor alloy film, e.g., above 80 at.% Mg, leads to widespread film cracking due to the removal of such a significant amount of the original material during dealloying and subsequent instability of the resulting free volume. Too much Mg in the precursor precludes attainment of the desired nanoporous structure after dealloying, as shown in Figure 3a,b. On the other hand, a significantly lower Mg content, e.g., 65 at.% Mg, proves to be insufficient for pore development and formation of a bicontinuous nanoporous structure, as shown in Figure 3c,d. This is attributed to Mg being effectively buried in the solid solution beneath refractory elements and therefore limiting the extent of dealloying that can occur and/or to the abundance of refractory elements that can diffuse at the elevated temperatures employed in thermal dealloying and thereby cover the sacrificial Mg. The film cracking observed in the dealloyed film created from a precursor that contained excessive Mg (Figure 3a,b) is similar to a phenomenon commonly observed in other dealloying methods, such as ECD and LMD [63,64]. Significant removal of material from a film that is attached to a substrate (which does not experience dealloying) can result in microscale void or crack formation [65] and, ultimately, film delamination [66]. Dealloying induces residual stress in the film, and this is typically tensile stress [63,67].

Because the lateral dimensions of the film are constrained by the substrate, the film can only shrink in thickness without experiencing cracking. The formation of cracks and voids can relieve the stress induced in the film during dealloying. However, from a practical perspective, it is often desirable to obtain crack-free nanoporous material.

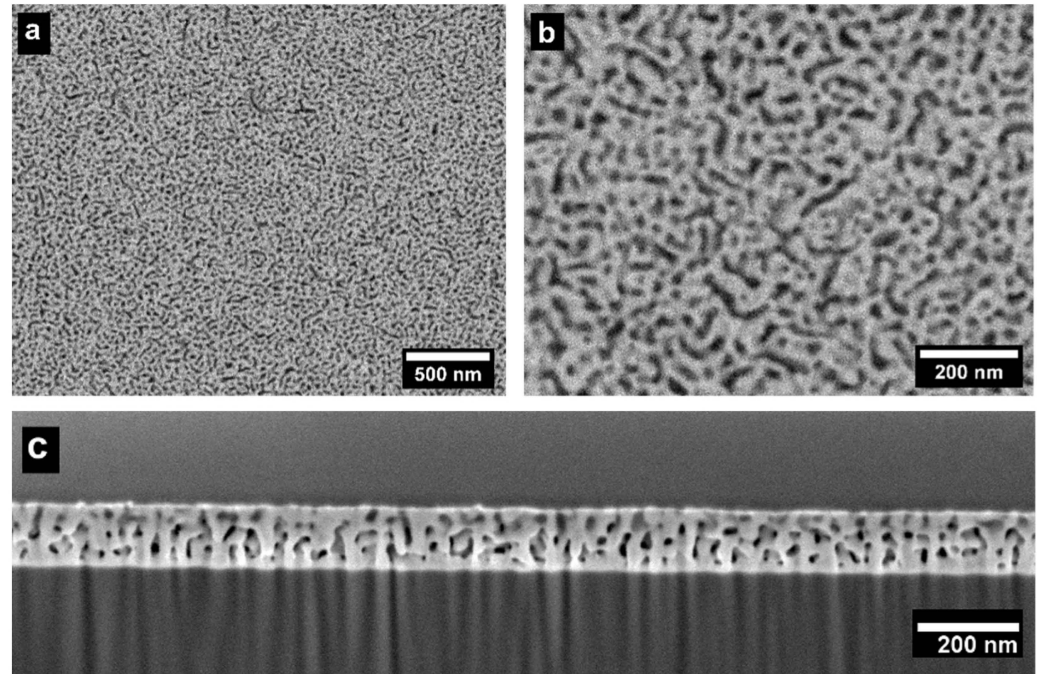


Figure 2. (a,b) Plan-view SEM micrographs of thermally dealloyed np-RMPEA thin films, showing the open porosity and interconnected ligaments in this nanoporous structure. (c) Cross-section SEM micrograph showing ligament structure through the thickness of the dealloyed film.

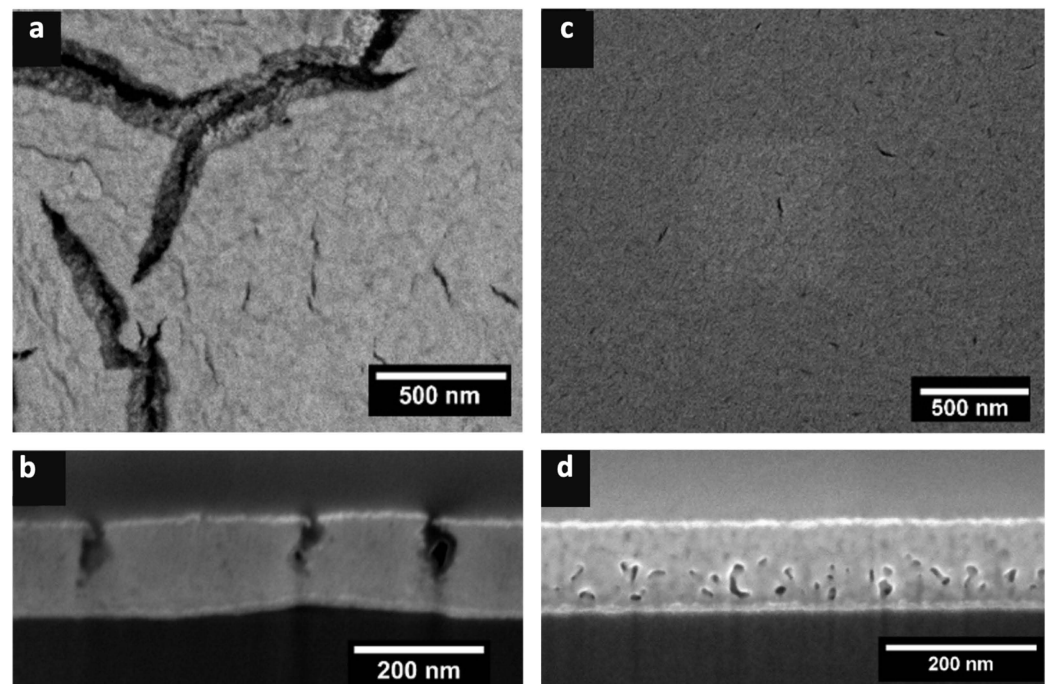


Figure 3. (a,b) SEM micrographs of the dealloyed structure from precursors that contained >80 at.% Mg, exhibiting cracks that extended from the film surface nearly to the substrate. (c,d) For a precursor that contained 65 at.% Mg, dealloying was suppressed, and a minimal amount of porosity was generated, limited to the bottom of the film near the substrate.

The optimized precursor alloy (VMoNbTa)₂₄Mg₇₆ strikes a balance between providing sufficient Mg to obtain the desired nanoporous structure via thermal dealloying while avoiding an overabundance of Mg that would lead to film cracking. Consequently, a crack-free film with np-structure closely resembling np-Au [68,69] was obtained.

After vacuum thermal dealloying, a significant portion of Mg from the (VMoNbTa)₂₄Mg₇₆ precursor was removed, leaving a low residual amount of Mg (<4 at.%). However, the relative proportions of refractory elements (V, Mo, Nb, Ta) before and after vacuum thermal dealloying (Table 1) remained nearly identical. This suggests that only Mg was removed from the precursor alloy, which is consistent with expectations based on the relative vapor pressures of all elements in the precursor.

Table 1. Alloy composition before and after dealloying, indicating that almost all Mg was removed. In addition to EDS analysis of all elements, alloy composition based on the refractory elements (only) showed that MPEA composition was not significantly affected by thermal dealloying.

Element	Precursor Film Composition (at.%)	Dealloyed Film Composition (at.%)	Precursor Film Composition with Refractory Elements Only (at.%)	Dealloyed Film Composition with Refractory Elements Only (at.%)
Mg	76.3	3.7	–	–
V	5.8	22.2	24.6	23.2
Mo	5.8	24.1	24.6	24.9
Nb	6.2	25.9	26.3	26.9
Ta	5.8	24.1	24.6	25

An XRD scan of the precursor thin film (Figure 4a) revealed a strongly textured (101) orientation of the hexagonal close-packed (HCP) crystal structure. Under bulk equilibrium conditions, V, Mo, Nb, and Ta all exhibit positive values for their binary enthalpies of mixing with Mg ($\Delta H^{\text{mix}}_{(\text{Mg-V/Mo/Nb/Ta})}$), indicating complete immiscibility with Mg. This can be verified via calculation using Miedema's model [50,70]. However, during the sputtering process, the deposited atoms impinge on the substrate quickly and are rapidly cooled, thereby preventing adatoms from relaxing into their lowest-energy state. As a result, phase separation between the refractory elements and Mg does not occur, and there is no evidence of separate phases in the XRD scan. This phenomenon was observed in similar thin films with high Mg content, such as Mg-Nb [71], where an analogous textured peak indicative of an HCP solid solution was reported. Another study [72] of thin film Mg on silicon substrate also exhibited the same (101) HCP texture. In contrast, an XRD scan of the dealloyed film (Figure 4b) indicated a single-phase body-centered cubic (BCC) structure, which is completely different from the highly textured HCP structure in the precursor. A single-phase structure is common and indeed desirable in certain MPEA or HEA systems [12,73,74].

Conversion of the HCP to BCC crystal structure occurs during dealloying via the ongoing simultaneous processes of Mg sublimation and ligament formation by the refractory elements (all of which crystallize in the BCC structure as bulk metals). As the sacrificial element (Mg) is removed from the precursor, the refractory elements V, Mo, Nb, and Ta remain on the dealloyed, exposed surface. These refractory surface atoms can minimize their energy by undergoing surface diffusion, reorganizing, and clustering together on the surface instead of remaining isolated as thermodynamically unstable adatoms. These atomic clusters grow by accretion of additional refractory metal atoms and eventually form randomly oriented ligaments that constitute the structure of the resultant nanoporous alloy. Because the clusters and ligaments typically form via the combination of freely moving adatoms undergoing surface diffusion, they crystallize in the lowest-energy crystal structure, which is the BCC structure, because all of the refractory elements prefer to exist as BCC crystals. The precursor alloy primarily contained Mg (>75 at.%), which prefers to

exist as an HCP metal. Because the precursor alloy was fabricated by thin film deposition and experienced non-equilibrium cooling conditions that exist during condensation from the physical vapor, the precursor alloy formed as an HCP solid solution, i.e., a metastable condition that is not consistent with equilibrium phase diagrams but is stabilized by the dominant Mg content. During dealloying, the refractory metal atoms were liberated into adatoms that subsequently agglomerated and formed the equilibrium BCC crystal structure.

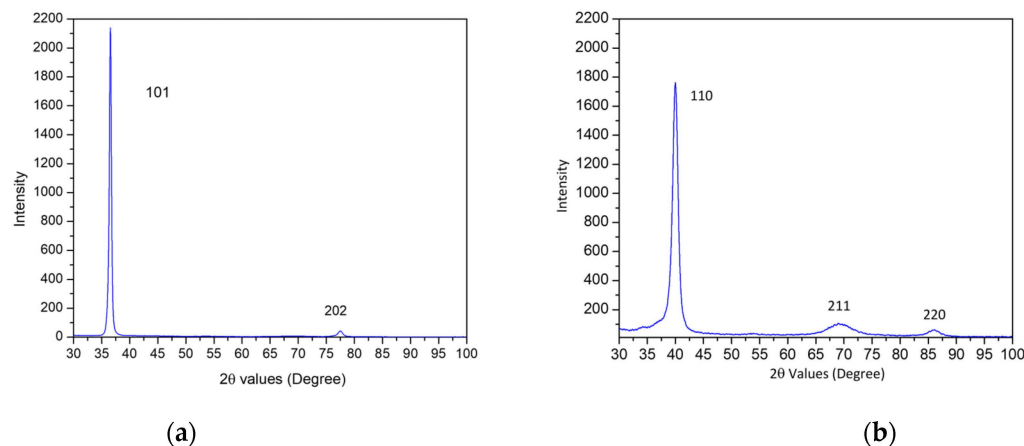


Figure 4. XRD scans before and after thermal dealloying. (a) The precursor alloy exhibits a strong (101) fiber texture corresponding to the HCP crystal structure (only). (b) The dealloyed film exhibits a (110) BCC fiber texture, with no remnants of the HCP Mg-based phase from the precursor.

The (110) BCC peak for the dealloyed film exhibited dominant intensity, indicating that it is the preferred crystallographic orientation that evolves during dealloying, i.e., np-RMPEA ligaments are oriented with a $\langle 110 \rangle$ VMoNbTa out-of-plane orientation. This may result from lattice coherency between the ligaments (as they form during thermal dealloying) and the underlying precursor alloy. The lattice parameter of the dealloyed np-RMPEA film, calculated as 3.201 Å from the XRD scan, closely matches the lattice parameter (3.202 Å) calculated by the rule of mixtures, including remnant Mg along with the refractory elements. This is also very close to the value reported in the literature for the equiatomic medium entropy alloy MoNbTaV (3.204 Å) [75], which has a similar composition to the alloy in the current study. The peak positions in XRD scans were determined using Origin software and a Gauss model for peak fitting. The standard errors in peak position (2θ) for the dealloyed sample were determined as 0.00645°, 0.008° and 0.00921°. This information was used to calculate the corresponding d-spacings and determine the bounding values of the lattice parameter for each peak. The maximum error associated with the lattice parameter calculations is 0.0005 Å. Only BCC peaks were observed in XRD scans of the np-MPEA, confirming the existence of a random solid solution of V, Mo, Nb, and Ta, and corroborating that Mg was (nearly) completely removed during dealloying.

3.2. Ligament Size Measurement and Time-Dependence of Ligament Coarsening

The evolution of ligament width in nanoporous structures is governed by surface diffusion and mobility of the more noble element(s) and, therefore, depends on the homologous temperature T_H [defined as $T(K)/T_{\text{melting}}(K)$] [76]. Materials with higher melting points have a lower T_H , thereby reducing the temperature-dependent diffusion rate at a given temperature. The refractory elements in the present study have relatively high melting points (V: 1910 °C, Mo: 2623 °C, Nb: 2477 °C, Ta: 3017 °C [58]). Thermal dealloying at 600 °C, therefore, results in low T_H values for the constituent refractory metal atoms. Consequently, these elements exhibit small ligament size due to slow diffusion rates [76,77]. Additionally, the formation of the MPEA further hinders diffusion due to atomic size differences among the constituent elements, leading to the formation of finer ligament size [50].

The average ligament size observed in the as-dealloyed film was 10 ± 2 nm, as shown in Figure 5. This is smaller than other values in the literature reported for nanoporous structures consisting of single refractory metals fabricated at a comparable dealloying temperature [57]. Similar ligament sizes at 600 °C have also been reported by Joo et al. [47] for TiVNbMoTa HEA nanoporous alloy fabricated by liquid metal dealloying. These findings suggest that nanoporous refractory MPEAs can effectively resist thermal coarsening at high temperatures by suppressing surface diffusion.

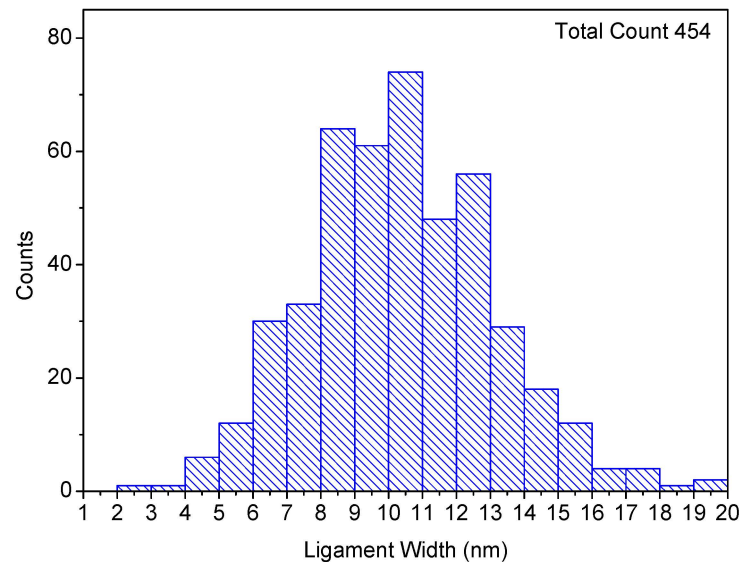


Figure 5. Ligament size distribution of np-RMPEA after vacuum thermal dealloying at 600 °C, with ligaments exhibiting an average width of 10 ± 2 nm. The size distribution was determined by measuring more than 400 ligaments in plan view as well as cross-section images.

The smaller ligament size observed for np-RMPEA specimens in the current study may result from the “sluggish diffusion” phenomenon that was postulated for MPEAs. A study by Tsai et al. [48] demonstrated slower diffusion in MPEAs, proposing that the atomic size mismatch in MPEAs induces fluctuations in lattice potential energy (LPE), resulting in the presence of lower potential energy sites that can hinder atomic diffusion. However, other researchers [78–80] did not find explicit evidence supporting “sluggish diffusion” as a core phenomenon in MPEAs. They argue that adding four or more elements does not necessarily produce the sluggish diffusion effect but rather that a particular element can contribute to the formation of a deep potential barrier that hinders diffusion. Nevertheless, there is currently no definitive consensus on the sluggish diffusion effect in BCC MPEAs. At T_H values similar to those in the current study, other researchers [79,81] observed relatively slow diffusion in MPEAs. Targeted studies specifically focusing on diffusion in the BCC MPEAs are needed to determine whether sluggish diffusion is a characteristic feature or not. In the current study, it is assumed that small atoms (such as V in this RMPEA) contribute to the presence of lower-energy LPE sites that hinder atomic motion.

Because it is governed by surface diffusion, ligament width evolution in np-RMPEAs should depend on temperature and duration of dealloying time. Remarkably, ligaments in the np-RMPEA studied here exhibited excellent stability and interconnectivity (Figure 6), even after being subjected to an elevated temperature of 700 °C for an extended period of 48 h. The average ligament width after annealing at various temperatures is listed in Table 2, where it is seen that heating for 48 h resulted in an average ligament size of 26 nm. Figure 7 shows a plot of ligament width vs. time, plotted on a logarithmic scale, for samples annealed at the same vacuum level. During the initial 10 h, the plot exhibits a linear relationship between $\ln(l)$ and $\ln(t)$, indicating that ligament growth during VTD and annealing is a thermally activated process. After 10 h, the slope (growth rate) decreases significantly and almost plateaus. This indicates that ligaments undergo minimal

coarsening beyond 10 h, further emphasizing the ability of this RMPEA to be stable against coarsening at high temperatures. By analyzing the initial region of the plot, the relationship between ligament width (l) and time (t) was found to be $l \propto t^{0.25}$. Coarsening processes can often be described by the relationship $d \propto t^{1/n}$ (where d is feature size, t is time, and n corresponds to the mechanism controlling coarsening) [82]. This would indicate that $n \sim 4$ for the RMPEA studied here, which is consistent with surface diffusion governing the coarsening process [82–84].

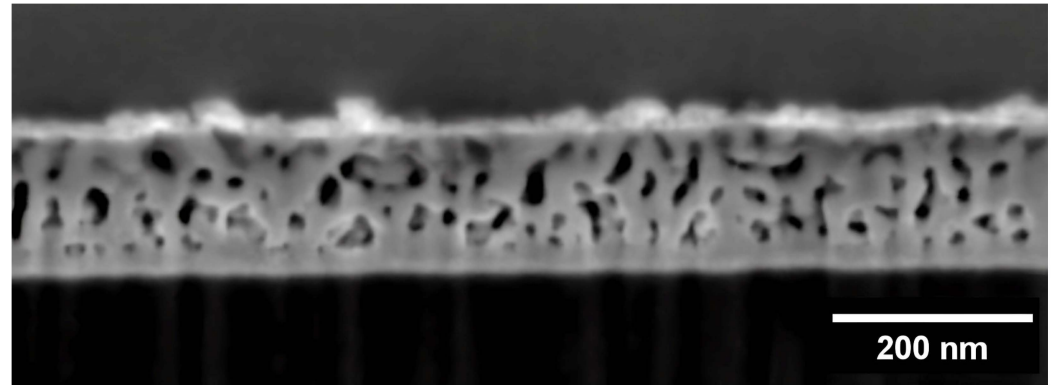


Figure 6. Cross-section SEM image of the np-RMPEA after annealing at 700 °C for 48 h. The nanoporous structure is highly interconnected, and ligaments are stable for long periods at elevated temperatures.

Table 2. Evolution of ligament width with time during thermal coarsening in the VTD chamber.

Time (h)	Average Ligament Width (nm)	Standard Deviation (nm)
1	15	±4
2	17	±4
3	19	±3
4	20	±5
5	21	±5
6	23	±4
8	23	±5
10	25	±5
20	25	±6
48	26	±5

Surface diffusivity, D_s , can be estimated from Equation (1) [82,85,86]:

$$D_s = \frac{l^4 K T}{32 \gamma t \alpha^4} \quad (1)$$

where D_s is surface diffusivity, l is ligament width, K is the Boltzmann constant ($1.3806 \times 10^{-23} \text{ JK}^{-1}$), T is absolute temperature, γ is surface energy calculated by rule of mixtures (2.404 Jm^{-2}) [87], t is annealing time, and α is the lattice parameter (3.201 \AA , as obtained from XRD). Based on the experimentally measured average ligament width $l = 10 \text{ nm}$ (and also considering 12 nm , which represents the upper end of the range of measured ligament widths) after thermal dealloying at $T = 873 \text{ K}$ for $t = 7200 \text{ s}$ (2 h), the diffusivity of np-VMoNbTa was calculated as $2.07 \times 10^{-16} \text{ cm}^2/\text{s}$ (and $4.2 \times 10^{-16} \text{ cm}^2/\text{s}$, respectively, for $l = 12 \text{ nm}$). Similarly, using the average ligament width $l = 25 \text{ nm}$ (and also 30 nm , representing the upper end of the ligament width range) after annealing at 973 K for $t = 172,800 \text{ s}$ (48 h), we obtain a diffusivity of $3.75 \times 10^{-16} \text{ cm}^2/\text{s}$ (and $7.8 \times 10^{-16} \text{ cm}^2/\text{s}$, respectively, for $l = 30 \text{ nm}$). Note that the initial dealloying time period was not included in the 700 °C annealing time, as those 2 h at 600 °C are roughly equivalent to 1 min at 700 °C . Both of the calculated values of surface diffusivity are significantly (1–2 orders of magnitude) lower than the diffusivity of Ta, which has the lowest surface diffusivity of the constituent

refractory elements [47]. This is reflected in Figure 8, where the calculated diffusivity values are compared to temperature-dependent values of surface diffusivity for each refractory metal based on relationships from the literature. Ta still has a diffusivity that is higher than that of the np-RMPEA by one order of magnitude or more.

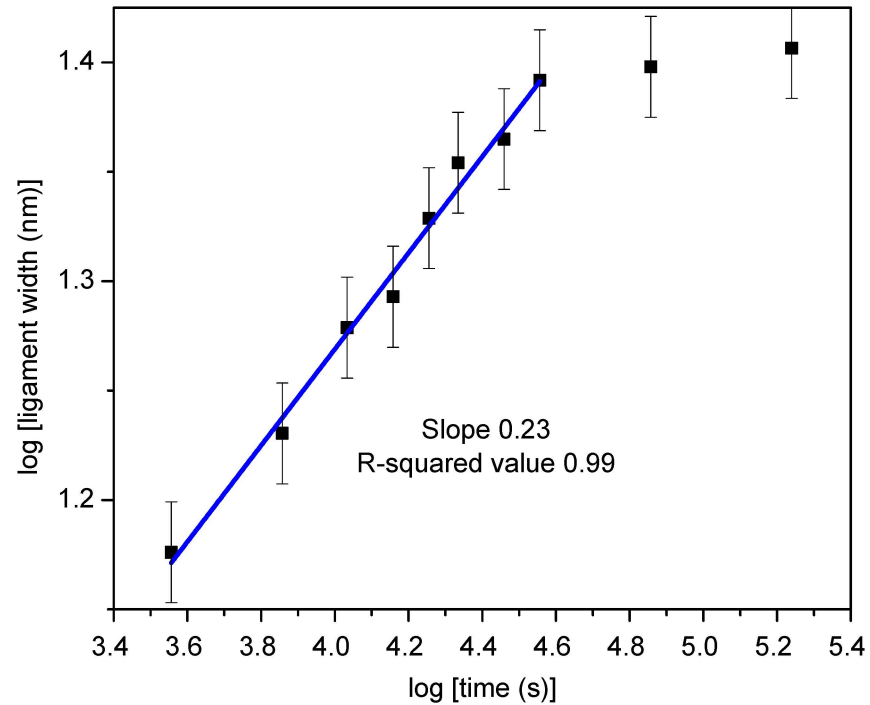


Figure 7. Logarithmic plot of ligament width l versus annealing time t , which exhibits the relationship $l \propto t^{0.25}$ during the first 10 h. This suggests that surface diffusion governs ligament coarsening, at least initially.

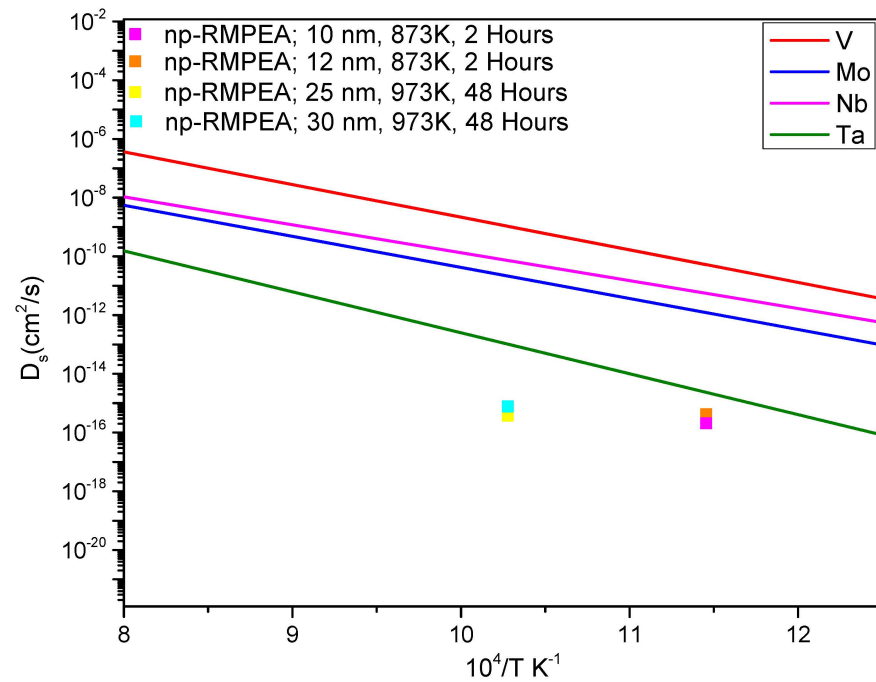


Figure 8. Calculated values of surface diffusivity for the np-RMPEA in the current study, as compared to the constituent refractory elements, indicating that the np-RMPEA exhibits slower diffusion kinetics. Surface diffusivity values for the pure metals were plotted using equations found in references [88–90].

Enhanced structural stability of np-RMPEAs enables them to retain high values of specific surface area, even after extended times at elevated temperatures. Figure 9 shows the evolution of specific surface area at 700 °C at different annealing times, calculated from the measured values of average ligament width. The specific surface area S is useful for comparing materials with different atomic weights or densities and can be estimated by assuming a disordered nanoporous structure and applying Equation (2) [91]:

$$S = \frac{C}{\rho_s \times l} \quad (2)$$

where C is a constant that depends on nanoporous structure, l is average ligament size, and ρ_s is bulk solid density. The value for ρ_s was calculated using a rule of mixtures approach and incorporated np-RMPEA composition along with the metallic radii of constituent metals and the lattice parameter determined using XRD. A value of $C = 3.7$ was used in the calculations and corresponds to a disordered nanoporous structure [91].

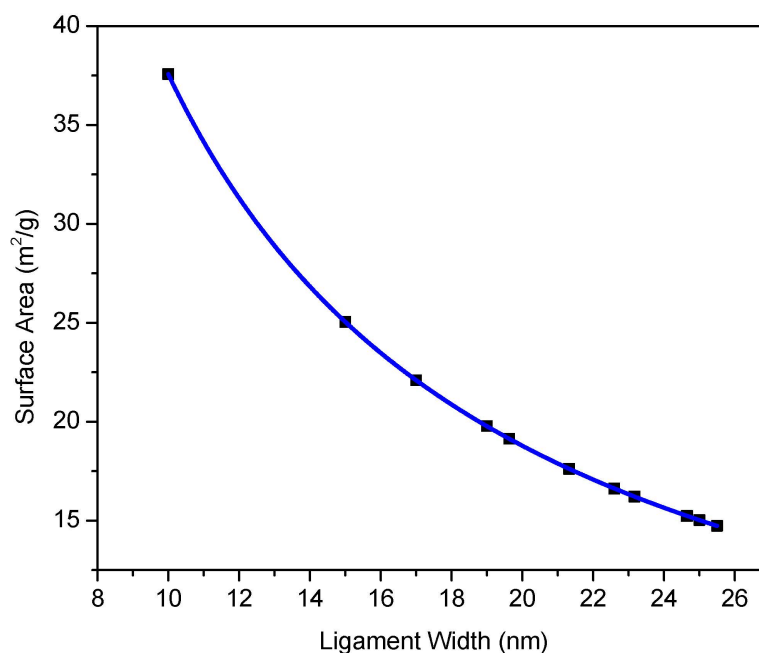


Figure 9. Relationship between specific surface area and ligament width. The np-RMPEA retained high surface area, even after long annealing times at high temperatures.

3.3. Depth Profiling

The VTD process is particularly suitable for materials that have a strong tendency to form oxides, such as refractory metals. The XPS depth profiling of the dealloyed sample was used to determine the elemental composition as a function of depth in the nanoporous film. A sequence of 20 incremental etching steps was executed, and an XPS scan was acquired after each etching step. The result indicated that np-VMoNbTa primarily consisted of metallic elements, albeit with a non-negligible degree of oxidation when analyzed after the VTD process. For simplification, the plot in Figure 10 represents total metal content (V + Mo + Nb + Ta with metallic bonding) compared to total metal oxide content (bonding between a refractory metal and oxygen). While the surface of the dealloyed film exhibited significant oxidation, the ligament cores (and therefore, the majority of the np structure that was exposed by etching steps during depth profiling) remained predominantly metallic, and this accounted for ~75% of the np-VMoNbTa volume. This agrees well with similar findings reported in the literature [57], corroborating the claim that VTD is effective for minimizing the oxidation of ligaments.

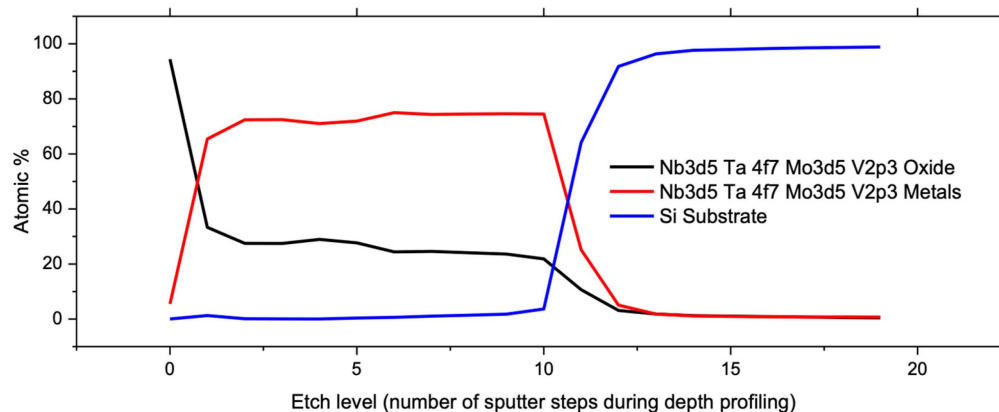


Figure 10. XPS depth profile of np-VMoNbTa, indicating that ligament cores are primarily metallicly bonded with a total metal content of 75%. This shows that VTD can mitigate the tendency of these refractory elements to oxidize during dealloying.

4. Conclusions

In this study, we employed a novel dealloying technique, vacuum thermal dealloying (VTD), to synthesize np-RMPEAs from a Mg-(VMoNbTa) precursor thin film that had been deposited using magnetron sputtering.

- By leveraging its significantly higher vapor pressure, Mg was almost completely removed from the precursor thin film. The precursor film exhibited the HCP crystal structure with a strong 101 texture, whereas the dealloyed np-RMPEA transformed to the BCC crystal structure. VTD of Mg-based precursor thin films resulted in a nanoporous structure featuring fine (10–12 nm) ligaments and no cracks.
- np-VMoNbTa exhibits smaller ligaments than corresponding elemental refractory np-metals, which can be attributed to the slow diffusion kinetics of RMPEAs. Surface diffusion in this np-RMPEA proved to be slower than in Ta, which has the slowest diffusion rate among the constituent refractory elements present in the alloy. This slow diffusion phenomenon enables np-VMoNbTa to retain excellent structural stability and fine ligament size (25–30 nm width) during high-temperature annealing for extended times.
- np-VMoNbTa fabricated by vacuum thermal dealloying experienced an intermediate degree of oxidation, especially compared to the constituent refractory metals, i.e., it was not oxidized to the degree that refractory metals would experience during chemical dealloying. This was confirmed by XPS, where the results were consistent with the ligament cores in the np-structure being predominantly metallic and the ligament surfaces being oxidized.

With its ability to produce fine ligaments that are thermally stable and resistant to oxidation, the VTD fabrication of np-VMoNbTa can potentially yield materials for service in high-temperature environments where a conventionally prepared np-material would experience structural instability due to ligament coarsening. More broadly, similar np-RMPEAs could offer enhanced performance in high-radiation environments, which may be the subject of future studies.

Author Contributions: Conceptualization, T.D.G. and T.J.B.; Formal analysis, T.D.G.; Funding acquisition, T.J.B.; Investigation, T.D.G.; Methodology, T.D.G. and T.J.B.; Project administration, T.J.B.; Writing—original draft, T.D.G.; Writing—review and editing, T.D.G. and T.J.B. All authors have read and agreed to the published version of the manuscript.

Funding: This work was supported by the U.S. Department of Energy, Office of Science, Basic Energy Sciences, under Award # DE-SC0019402.

Data Availability Statement: The raw data supporting the conclusions of this article will be made available by the authors on request.

Acknowledgments: Access to electron microscopy and related equipment was provided by the Electron Microscopy Center at the University of Kentucky, a member of the National Nanotechnology Coordinated Infrastructure (NNCI), which is supported by the National Science Foundation (ECCS-1542164).

Conflicts of Interest: The authors declare no conflicts of interest.

References

1. Pergher, S.B.C.; Rodríguez-Castellón, E. Nanoporous Materials and Their Applications. *Appl. Sci.* **2019**, *9*, 1314. [CrossRef]
2. Gan, Y.X.; Zhang, Y.; Gan, J.B. Nanoporous Metals Processed by Dealloying and Their Applications. *AIMS Mater. Sci.* **2018**, *5*, 1141–1183. [CrossRef]
3. Ameen, S.; Akhtar, M.S.; Godbole, R.; Shin, H.-S. An Introduction to Nanoporous Materials. In *Nanofluid Flow in Porous Media*; 2019. Available online: <https://api.semanticscholar.org/CorpusID:139317302> (accessed on 20 February 2024).
4. Vizoso, D.; Kosmidou, M.; Balk, T.J.; Hattar, K.; Deo, C.; Dingreville, R. Size-Dependent Radiation Damage Mechanisms in Nanowires and Nanoporous Structures. *Acta Mater.* **2021**, *215*, 117018. [CrossRef]
5. Xu, H.; He, L.-L.; Pei, Y.-F.; Jiang, C.-Z.; Li, W.-Q.; Xiao, X.-H. Recent Progress of Radiation Response in Nanostructured Tungsten for Nuclear Application. *Tungsten* **2021**, *3*, 20–37. [CrossRef]
6. Hu, Z.Y.; Xu, C.; Liang, Y.X.; Yan, Y.; Yang, K.J.; Liu, Z.L.; Wang, X.J.; Fu, E.G. The Radiation Effect of Ion Species on the Microstructure of Nanoporous Gold. *Scr. Mater.* **2021**, *190*, 136–140. [CrossRef]
7. Lionello, D.F.; Ramallo, J.I.; Caro, M.; Wang, Y.Q.; Sheehan, C.; Baldwin, J.K.; Nogan, J.; Caro, A.; Fuertes, M.C.; Ruestes, C.J. Mechanical Properties of Al₂O₃-Functionalized Nanoporous Gold Foams under Irradiation. *J. Mater. Res.* **2021**, *36*, 2001–2009. [CrossRef]
8. Rugolo, J.; Erlebacher, J.; Sieradzki, K. Length Scales in Alloy Dissolution and Measurement of Absolute Interfacial Free Energy. *Nat. Mater.* **2006**, *5*, 946–949. [CrossRef]
9. Erlebacher, J.; Aziz, M.J.; Karma, A.; Dimitrov, N.; Sieradzki, K. Evolution of Nanoporosity in Dealloying. *Nature* **2001**, *410*, 450–453. [CrossRef]
10. Li, Z.; Lu, X. Nanoindentation for Mechanical Behaviour Characterization of Nanoporous Silver Fabricated through Dealloying. *Bull. Mater. Sci.* **2021**, *44*, 149. [CrossRef]
11. Morrish, R.; Dorame, K.; Muscat, A.J. Formation of Nanoporous Au by Dealloying AuCu Thin Films in HNO₃. *Scr. Mater.* **2011**, *64*, 856–859. [CrossRef]
12. Yeh, J.-W.; Chen, S.-K.; Lin, S.-J.; Gan, J.-Y.; Chin, T.-S.; Shun, T.-T.; Tsau, C.-H.; Chang, S.-Y. Nanostructured High-Entropy Alloys with Multiple Principal Elements: Novel Alloy Design Concepts and Outcomes. *Adv. Eng. Mater.* **2004**, *6*, 299–303. [CrossRef]
13. Ter-Isahakyan, A. Derivation, Exploration and Evaluation of Non-Equiatomic High Entropy Alloys. Ph.D. Thesis, University of Kentucky, Lexington, KY, USA, 2022. [CrossRef]
14. Zhang, Z.; Mao, M.M.; Wang, J.; Gludovatz, B.; Zhang, Z.; Mao, S.X.; George, E.P.; Yu, Q.; Ritchie, R.O. Nanoscale Origins of the Damage Tolerance of the High-Entropy Alloy CrMnFeCoNi. *Nat. Commun.* **2015**, *6*, 10143. [CrossRef] [PubMed]
15. Lee, C.; Song, G.; Gao, M.C.; Feng, R.; Chen, P.; Brechtel, J.; Chen, Y.; An, K.; Guo, W.; Poplawsky, J.D.; et al. Lattice Distortion in a Strong and Ductile Refractory High-Entropy Alloy. *Acta Mater.* **2018**, *160*, 158–172. [CrossRef]
16. Liu, D.; Yu, Q.; Kabra, S.; Jiang, M.; Forna-Kreutzer, P.; Zhang, R.; Payne, M.; Walsh, F.; Gludovatz, B.; Asta, M.; et al. Exceptional Fracture Toughness of CrCoNi-Based Medium- and High-Entropy Alloys at 20 Kelvin. *Science* **2022**, *378*, 978–983. [CrossRef] [PubMed]
17. Fan, X.J.; Qu, R.T.; Zhang, Z.F. Remarkably High Fracture Toughness of HfNbTaTiZr Refractory High-Entropy Alloy. *J. Mater. Sci. Technol.* **2022**, *123*, 70–77. [CrossRef]
18. Li, W.; Wang, G.; Wu, S.; Liaw, P.K. Creep, Fatigue, and Fracture Behavior of High-Entropy Alloys. *J. Mater. Res.* **2018**, *33*, 3011–3034. [CrossRef]
19. Sahragard-Monfared, G.; Zhang, M.; Smith, T.M.; Minor, A.M.; Gibeling, J.C. Superior Tensile Creep Behavior of a Novel Oxide Dispersion Strengthened CrCoNi Multi-Principal Element Alloy. *Acta Mater.* **2023**, *255*, 119032. [CrossRef]
20. Sahragard-Monfared, G.; Zhang, M.; Smith, T.M.; Minor, A.M.; George, E.P.; Gibeling, J.C. The Influence of Processing Methods on Creep of Wrought and Additively Manufactured CrCoNi Multi-Principal Element Alloys. *Acta Mater.* **2023**, *261*, 119403. [CrossRef]
21. Qiu, Y.; Thomas, S.; Gibson, M.A.; Fraser, H.L.; Birbilis, N. Corrosion of High Entropy Alloys. *NPJ Mater. Degrad.* **2017**, *1*, 15. [CrossRef]
22. Fu, Y.; Li, J.; Luo, H.; Du, C.; Li, X. Recent Advances on Environmental Corrosion Behavior and Mechanism of High-Entropy Alloys. *J. Mater. Sci. Technol.* **2021**, *80*, 217–233. [CrossRef]
23. Ouyang, G.; Singh, P.; Su, R.; Johnson, D.D.; Kramer, M.J.; Perepezko, J.H.; Senkov, O.N.; Miracle, D.; Cui, J. Design of Refractory Multi-Principal-Element Alloys for High-Temperature Applications. *NPJ Comput. Mater.* **2023**, *9*, 141. [CrossRef]
24. Wang, J.; Jiang, H.; Chang, X.; Zhang, L.; Wang, H.; Zhu, L.; Qin, S. Effect of Cu Content on the Microstructure and Corrosion Resistance of AlCrFeNi₃Cu_x High Entropy Alloys. *Corros. Sci.* **2023**, *221*, 111313. [CrossRef]
25. Xia, S.Q.; Yang, X.; Yang, T.F.; Liu, S.; Zhang, Y. Irradiation Resistance in Al_xCoCrFeNi High Entropy Alloys. *JOM* **2015**, *67*, 2340–2344. [CrossRef]

26. Deluigi, O.R.; Pasianot, R.C.; Valencia, F.J.; Caro, A.; Farkas, D.; Bringa, E.M. Simulations of Primary Damage in a High Entropy Alloy: Probing Enhanced Radiation Resistance. *Acta Mater.* **2021**, *213*, 116951. [CrossRef]
27. Cheng, Z.; Sun, J.; Gao, X.; Wang, Y.; Cui, J.; Wang, T.; Chang, H. Irradiation Effects in High-Entropy Alloys and Their Applications. *J. Alloys Compd.* **2023**, *930*, 166768. Available online: <https://www.sciencedirect.com/science/article/pii/S0925838822031590> (accessed on 20 February 2024). [CrossRef]
28. Yu, Y.; Yu, Y. Simulations of Irradiation Resistance and Mechanical Properties under Irradiation of High-Entropy Alloy NiCoCrFe. *Mater. Today Commun.* **2022**, *33*, 104308. [CrossRef]
29. Abid, T.; Akram, M.A.; Yaqub, T.B.; Ramzan Abdul Karim, M.; Fernandes, F.; Zafar, M.F.; Yaqoob, K. Design and Development of Porous CoCrFeNiMn High Entropy Alloy (Cantor Alloy) with Outstanding Electrochemical Properties. *J. Alloys Compd.* **2024**, *970*, 172633. [CrossRef]
30. Yu, Z.-Y.; Sun, Q.; Li, H.; Qiao, Z.-J.; Li, W.-J.; Chou, S.-L.; Zhang, Z.-J.; Jiang, Y. Tuning Single-Phase Medium-Entropy Oxides Derived from Nanoporous NiCuCoMn Alloy as a Highly Stable Anode for Li-Ion Batteries. *Rare Met.* **2023**, *42*, 2982–2992. [CrossRef]
31. Yu, T.; Zhang, Y.; Hu, Y.; Hu, K.; Lin, X.; Xie, G.; Liu, X.; Reddy, K.M.; Ito, Y.; Qiu, H.-J. Twelve-Component Free-Standing Nanoporous High-Entropy Alloys for Multifunctional Electrocatalysis. *ACS Mater. Lett.* **2022**, *4*, 181–189. [CrossRef]
32. Cai, Z.-X.; Goou, H.; Ito, Y.; Tokunaga, T.; Miyachi, M.; Abe, H.; Fujita, T. Nanoporous Ultra-High-Entropy Alloys Containing Fourteen Elements for Water Splitting Electrocatalysis. *Chem. Sci.* **2021**, *12*, 11306–11315. [CrossRef]
33. Wei, Y.; Zhao, Y.; Chen, Y.; Zhang, M.; Zhang, Z.; Kang, J.; Ma, X.; Jiang, Y.; Zhang, Y. Lithium Storage Characteristic of Nanoporous High-Entropy Alloy@high-Entropy Oxide with Spin-Dependent Synergism of Cations. *Chem. Eng. J.* **2023**, *476*, 146881. [CrossRef]
34. Liu, H.; Qin, H.; Kang, J.; Ma, L.; Chen, G.; Huang, Q.; Zhang, Z.; Liu, E.; Lu, H.; Li, J.; et al. A Freestanding Nanoporous NiCoFeMoMn High-Entropy Alloy as an Efficient Electrocatalyst for Rapid Water Splitting. *Chem. Eng. J.* **2022**, *435*, 134898. [CrossRef]
35. Qiu, H.-J.; Fang, G.; Wen, Y.; Liu, P.; Xie, G.; Liu, X.; Sun, S. Nanoporous High-Entropy Alloys for Highly Stable and Efficient Catalysts. *J. Mater. Chem. A* **2019**, *7*, 6499–6506. [CrossRef]
36. Li, S.; Tang, X.; Jia, H.; Li, H.; Xie, G.; Liu, X.; Lin, X.; Qiu, H.-J. Nanoporous High-Entropy Alloys with Low Pt Loadings for High-Performance Electrochemical Oxygen Reduction. *J. Catal.* **2020**, *383*, 164–171. [CrossRef]
37. Liu, L.-H.; Li, N.; Han, M.; Han, J.-R.; Liang, H.-Y. Scalable Synthesis of Nanoporous High Entropy Alloys for Electrocatalytic Oxygen Evolution. *Rare Met.* **2022**, *41*, 125–131. [CrossRef]
38. Lin, X.; Hu, Y.; Hu, K.; Lin, X.; Xie, G.; Liu, X.; Reddy, K.M.; Qiu, H.-J. Inhibited Surface Diffusion of High-Entropy Nano-Alloys for the Preparation of 3D Nanoporous Graphene with High Amounts of Single Atom Dopants. *ACS Mater. Lett.* **2022**, *4*, 978–986. [CrossRef]
39. Zhao, C.; Cai, W.; Sun, N.; Chen, S.; Jing, W.; Zhao, C. Facile Preparation of Porous High-Entropy Alloy FeCoNiCuMn and Its OER Performance. *J. Phys. Chem. Solids* **2024**, *184*, 111668. [CrossRef]
40. Yao, R.-Q.; Zhou, Y.-T.; Shi, H.; Wan, W.-B.; Zhang, Q.-H.; Gu, L.; Zhu, Y.-F.; Wen, Z.; Lang, X.-Y.; Jiang, Q. Nanoporous Surface High-Entropy Alloys as Highly Efficient Multisite Electrocatalysts for Nonacidic Hydrogen Evolution Reaction. *Adv. Funct. Mater.* **2021**, *31*, 2009613. [CrossRef]
41. Shi, H.; Sun, X.-Y.; Zeng, S.-P.; Liu, Y.; Han, G.-F.; Wang, T.-H.; Wen, Z.; Fang, Q.-R.; Lang, X.-Y.; Jiang, Q. Nanoporous Nonprecious High-Entropy Alloys as Multisite Electrocatalysts for Ampere-Level Current-Density Hydrogen Evolution. *Small Struct.* **2023**, *4*, 2300042. [CrossRef]
42. Wang, Y.; Yu, B.; He, M.; Zhai, Z.; Yin, K.; Kong, F.; Zhang, Z. Eutectic-Derived High-Entropy Nanoporous Nanowires for Efficient and Stable Water-to-Hydrogen Conversion. *Nano Res.* **2022**, *15*, 4820–4826. [CrossRef]
43. Biener, J.; Hodge, A.M.; Hayes, J.R.; Volkert, C.A.; Zepeda-Ruiz, L.A.; Hamza, A.V.; Abraham, F.F. Size Effects on the Mechanical Behavior of Nanoporous Au. *Nano Lett.* **2006**, *6*, 2379–2382. [CrossRef]
44. Fujita, T.; Tokunaga, T.; Zhang, L.; Li, D.; Chen, L.; Arai, S.; Yamamoto, Y.; Hirata, A.; Tanaka, N.; Ding, Y.; et al. Atomic Observation of Catalysis-Induced Nanopore Coarsening of Nanoporous Gold. *Nano Lett.* **2014**, *14*, 1172–1177. [CrossRef]
45. Jeon, H.; Woo, J.-H.; Song, E.; Kim, J.-Y. Ligament Size Effect in Creep of Nanoporous Gold. *Int. J. Plast.* **2022**, *150*, 103192. [CrossRef]
46. Saffarini, M.H.; Voyiadjis, G.Z.; Ruestes, C.J. Scaling Laws for Nanoporous Metals under Uniaxial Loading. *J. Mater. Res.* **2021**, *36*, 2729–2741. [CrossRef]
47. Joo, S.-H.; Bae, J.W.; Park, W.-Y.; Shimada, Y.; Wada, T.; Kim, H.S.; Takeuchi, A.; Konno, T.J.; Kato, H.; Okulov, I.V. Nanoporous Materials: Beating Thermal Coarsening in Nanoporous Materials via High-Entropy Design. *Adv. Mater.* **2020**, *32*, 2070044. [CrossRef]
48. Tsai, K.-Y.; Tsai, M.-H.; Yeh, J.-W. Sluggish Diffusion in Co–Cr–Fe–Mn–Ni High-Entropy Alloys. *Acta Mater.* **2013**, *61*, 4887–4897. [CrossRef]
49. Joo, S.-H.; Kato, H.; Okulov, I.V. Evolution of 3D Interconnected Composites of High-Entropy TiVNbMoTa Alloys and Mg during Liquid Metal Dealloying. *Compos. Part B Eng.* **2021**, *222*, 109044. [CrossRef]
50. Okulov, A.V.; Joo, S.-H.; Kim, H.S.; Kato, H.; Okulov, I.V. Nanoporous High-Entropy Alloy by Liquid Metal Dealloying. *Metals* **2020**, *10*, 1396. [CrossRef]

51. El-Atwani, O.; Li, N.; Li, M.; Devaraj, A.; Baldwin, J.K.S.; Schneider, M.M.; Sobieraj, D.; Wróbel, J.S.; Nguyen-Manh, D.; Maloy, S.A.; et al. Outstanding Radiation Resistance of Tungsten-Based High-Entropy Alloys. *Sci. Adv.* **2019**, *5*, eaav2002. [CrossRef]
52. Plasma-Wall Interaction with Irradiated Tungsten and Tungsten Alloys in Fusion Devices. Available online: <https://www.iaea.org/projects/crp/f43021> (accessed on 20 April 2021).
53. Basu, I.; De Hosson, J.T.M. High Entropy Alloys: Ready to Set Sail? *Metals* **2020**, *10*, 194. [CrossRef]
54. Xin, Y.; Li, S.; Qian, Y.; Zhu, W.; Yuan, H.; Jiang, P.; Guo, R.; Wang, L. High-Entropy Alloys as a Platform for Catalysis: Progress, Challenges, and Opportunities. *ACS Catal.* **2020**, *10*, 11280–11306. [CrossRef]
55. Tomboc, G.M.; Kwon, T.; Joo, J.; Lee, K. High Entropy Alloy Electrocatalysts: A Critical Assessment of Fabrication and Performance. *J. Mater. Chem. A* **2020**, *8*, 14844–14862. [CrossRef]
56. Lu, Z.; Zhang, F.; Wei, D.; Han, J.; Xia, Y.; Jiang, J.; Zhong, M.; Hirata, A.; Watanabe, K.; Karma, A.; et al. Vapor Phase Dealloying Kinetics of MnZn Alloys. *Acta Mater.* **2021**, *212*, 116916. [CrossRef]
57. Kosmidou, M.; Detisch, M.J.; Maxwell, T.L.; Balk, T.J. Vacuum thermal dealloying of magnesium-based alloys for fabrication of nanoporous refractory metals. *MRS Commun.* **2019**, *9*, 144–149. [CrossRef]
58. CRC Press. *CRC Handbook of Chemistry and Physics a Ready-Reference Book of Chemical and Physical Data*, 101st ed.; CRC Press Taylor & Francis Group: Boca Raton, FL, USA, 2020.
59. Rapson, W.S. Intermetallic Compounds of Gold. *Gold Bull.* **1996**, *29*, 141–142. [CrossRef]
60. Artymowicz, D.M.; Erlebacher, J.; Newman, R.C. Relationship between the Parting Limit for De-Alloying and a Particular Geometric High-Density Site Percolation Threshold. *Philos. Mag.* **2009**, *89*, 1663–1693. [CrossRef]
61. McCue, I.; Benn, E.; Gaskey, B.; Erlebacher, J. Dealloying and Dealloyed Materials. *Annu. Rev. Mater. Res.* **2016**, *46*, 263–286. [CrossRef]
62. Newman, R.C. 2.05—Dealloying. In *Shreir's Corrosion*; Cottis, B., Graham, M., Lindsay, R., Lyon, S., Richardson, T., Scantlebury, D., Stott, H., Eds.; Elsevier: Oxford, UK, 2010; pp. 801–809. ISBN 978-0-444-52787-5.
63. Seker, E.; Reed, M.L.; Begley, M.R. A Thermal Treatment Approach to Reduce Microscale Void Formation in Blanket Nanoporous Gold Films. *Scr. Mater.* **2009**, *60*, 435–438. [CrossRef]
64. Ma, Y.; Zhan, Z.; Tao, L.; Xu, G.; Tang, A.; Ouyang, T. Construction of MnO₂/Micro-Nano Ni-Filled Ni Foam for High-Performance Supercapacitors Application. *Ionics* **2020**, *26*, 4671–4684. [CrossRef]
65. Cialone, M.; Celegato, F.; Scaglione, F.; Barrera, G.; Raj, D.; Coisson, M.; Tiberto, P.; Rizzi, P. Nanoporous FePd Alloy as Multifunctional Ferromagnetic SERS-Active Substrate. *Appl. Surf. Sci.* **2021**, *543*, 148759. [CrossRef]
66. Henkelmann, G.; Waldow, D.; Liu, M.; Lührs, L.; Li, Y.; Weissmüller, J. Self-Detachment and Subsurface Densification of Dealloyed Nanoporous Thin Films. *Nano Lett.* **2022**, *22*, 6787–6793. [CrossRef] [PubMed]
67. Liu, R.; Antoniou, A. A Relation between Relative Density, Alloy Composition and Sample Shrinkage for Nanoporous Metal Foams. *Scr. Mater.* **2012**, *67*, 923–926. [CrossRef]
68. Dong, H.; Cao, X. Nanoporous Gold Thin Film: Fabrication, Structure Evolution, and Electrocatalytic Activity. *J. Phys. Chem. C* **2008**, *113*, 603–609. [CrossRef]
69. Briot, N. Nanomechanical And Scaling Behavior of Nanoporous Gold. Ph.D. Thesis, University of Kentucky, Lexington, KY, USA, 2015.
70. Miedema, A.R. Simple Model for Alloys. *Philips Tech. Rev.* **1973**, *33*, 149–160.
71. Staišiušas, L.; Leinartas, K.; Samulevičienė, M.; Miečinskis, P.; Griguševičienė, A.; Juškėnas, R.; Juzeliūnas, E. Electrochemical and Structural Characterization of Sputter-Deposited Mg–Nb and Mg–Nb–Al–Zn Alloy Films. *J. Solid State Electrochem.* **2013**, *17*, 1649–1656. [CrossRef]
72. Gordin, A.S.; Sandhage, K.H. In Situ High-Temperature X-Ray Diffraction Analysis of Mg₂Si Formation Kinetics via Reaction of Mg Films with Si Single Crystal Substrates. *Intermetallics* **2018**, *94*, 200–209. [CrossRef]
73. Cantor, B. Multicomponent and High Entropy Alloys. *Entropy* **2014**, *16*, 4749–4768. [CrossRef]
74. Cantor, B.; Chang, I.T.H.; Knight, P.; Vincent, A.J.B. Microstructural Development in Equiatomic Multicomponent Alloys. *Mater. Sci. Eng. A* **2004**, *375–377*, 213–218. [CrossRef]
75. Yao, H.; Qiao, J.-W.; Gao, M.C.; Hawk, J.A.; Ma, S.-G.; Zhou, H. MoNbTaV Medium-Entropy Alloy. *Entropy* **2016**, *18*, 189. [CrossRef]
76. McCue, I.; Karma, A.; Erlebacher, J. Pattern Formation during Electrochemical and Liquid Metal Dealloying. *MRS Bull.* **2018**, *43*, 27–34. [CrossRef]
77. Chen, Q.; Sieradzki, K. Mechanisms and Morphology Evolution in Dealloying. *Electrochem. Soc.* **2013**, *160*, C226–C231. [CrossRef]
78. Divinski, S.V.; Pokoev, A.; Esakiraja, N.; Paul, A. A Mystery of “Sluggish Diffusion” in High-Entropy Alloys: The Truth or a Myth? *arXiv* **2018**, arXiv:1804.03465. [CrossRef]
79. Kucza, W.; Dąbrowa, J.; Cieślak, G.; Berent, K.; Kulik, T.; Danielewski, M. Studies of “Sluggish Diffusion” Effect in Co–Cr–Fe–Mn–Ni, Co–Cr–Fe–Ni and Co–Fe–Mn–Ni High Entropy Alloys; Determination of Tracer Diffusivities by Combinatorial Approach. *J. Alloys Compd.* **2018**, *731*, 920–928. [CrossRef]
80. Verma, V.; Tripathi, A.; Venkateswaran, T.; Kulkarni, K.N. First Report on Entire Sets of Experimentally Determined Interdiffusion Coefficients in Quaternary and Quinary High-Entropy Alloys. *J. Mater. Res.* **2020**, *35*, 162–171. [CrossRef]
81. Dąbrowa, J.; Zajusz, M.; Kucza, W.; Cieślak, G.; Berent, K.; Czeppe, T.; Kulik, T.; Danielewski, M. Demystifying the Sluggish Diffusion Effect in High Entropy Alloys. *J. Alloys Compd.* **2019**, *783*, 193–207. [CrossRef]

82. Qian, L.H.; Chen, M.W. Ultrafine Nanoporous Gold by Low-Temperature Dealloying and Kinetics of Nanopore Formation. *Appl. Phys. Lett.* **2007**, *91*, 083105. [[CrossRef](#)]
83. Lu, Z.; Li, C.; Han, J.; Zhang, F.; Liu, P.; Wang, H.; Wang, Z.; Cheng, C.; Chen, L.; Hirata, A.; et al. Three-Dimensional Bicontinuous Nanoporous Materials by Vapor Phase Dealloying. *Nat. Commun.* **2018**, *9*, 276. [[CrossRef](#)]
84. Chen-Wiegart, Y.K.; Wang, S.; Chu, Y.S.; Liu, W.; McNulty, I.; Voorhees, P.W.; Dunand, D.C. Structural Evolution of Nanoporous Gold during Thermal Coarsening. *Acta Mater.* **2012**, *60*, 4972–4981. [[CrossRef](#)]
85. Liu, W.; Cheng, P.; Yan, J.; Li, N.; Shi, S.; Zhang, S. Temperature-Induced Surface Reconstruction and Interface Structure Evolution on Ligament of Nanoporous Copper. *Sci. Rep.* **2018**, *8*, 447. [[CrossRef](#)]
86. Andreasen, G.; Nazzarro, M.; Ramirez, J.; Salvarezza, R.C.; Arvia, A.J. Kinetics of Particle Coarsening at Gold Electrode/Electrolyte Solution Interfaces Followed by In Situ Scanning Tunneling Microscopy. *J. Electrochem. Soc.* **1996**, *143*, 466–471. [[CrossRef](#)]
87. Tyson, W.R.; Miller, W.A. Surface Free Energies of Solid Metals: Estimation from Liquid Surface Tension Measurements. *Surf. Sci.* **1977**, *62*, 267–276. [[CrossRef](#)]
88. Allen, B.C. The Surface Self-Diffusion of Mo, Cb (Nb), and Re. *Met. Mater Trans. B* **1972**, *3*, 2544–2547. [[CrossRef](#)]
89. Hok, S.; Drechsler, M. A Measurement of the Surface Self-Diffusion of Tantalum. *Surf. Sci. Lett.* **1981**, *107*, L362–L366. [[CrossRef](#)]
90. Yu, J.M.; Trivedi, R. Surface Self-Diffusion Studies on the (111) Surface of Vanadium. *Surf. Sci.* **1983**, *125*, 396–408. [[CrossRef](#)]
91. Detsi, E.; Jong, E.D.; Zinchenko, A.; Vukovic, Z.; Vukovic, I.; Punzhin, S.; Loos, K.; Brinke, G.; Raedt, H.A.D.; Onck, P.R.; et al. On the Specific Surface Area of Nanoporous Materials. *Acta Mater.* **2011**, *59*, 7488–7497. [[CrossRef](#)]

Disclaimer/Publisher’s Note: The statements, opinions and data contained in all publications are solely those of the individual author(s) and contributor(s) and not of MDPI and/or the editor(s). MDPI and/or the editor(s) disclaim responsibility for any injury to people or property resulting from any ideas, methods, instructions or products referred to in the content.